Formation and Propagation of Buckles in Coilable Cylindrical Thin Shells with a Thickness Discontinuity

Wen Luo, Sergio Pellegrino*

Graduate Aerospace Laboratories, California Institute of Technology
1200 E California Blvd, Pasadena, CA 91125, USA

Abstract

This paper studies the snap-through buckling that occurs ahead of the coiled region in thin, linear-elastic, isotropic coilable cylindrical shells with a sudden change in the thickness of the shell cross section. The study is focused on Triangular Rollable And Collapsible (TRAC) booms. It is shown that coiling of these shells leads to longitudinal compression of the inner flange mid-surface, which in turn leads to the formation of a buckle in the transition region between the fully coiled and fully deployed parts of the inner flange. This buckle grows to reach a steady-state configuration and is then pushed along the shell without changing its shape when the shell is coiled.

Keywords: Buckling, Deployable Structures, Thin shells

1. Introduction

Thin sheets of paper, textiles, metal, or plastic are coiled for continuous manufacture and compact storage. Their coiling mechanics have been extensively studied (Good and Roisum, 2008; Miura and Pellegrino, 2020) and it

---

*Corresponding author: sergiop@caltech.edu

is known that excessive tension, torque, or speed, can lead to coiling defects that include curled webs, ridges, starring, and internal wrinkles and buckles (Roisum, 1984). In a related class of problems, known as propagating instabilities, a localized instability propagates spontaneously under load control, driving a whole structure into a buckled configuration. Problems of this type include the initiation and propagation of bulges in rubber balloons and steel pipelines, described in the review paper by Kyriakides (1993). They also include the localization and propagation of buckles in cylindrical panels loaded by pressure (Power and Kyriakides, 1994).

The problem studied in the present paper is the buckling that occurs ahead of the coiled region in thin, coilable cylindrical shells with certain specific features. This buckle grows to reach a steady-state configuration and is then pushed along the shell, without changing shape, as the shell is further coiled. This problem also belongs to the category of propagating instabilities although its propagation is not spontaneous.

The particular type of shell that is of interest is the Triangular Rollable And Collapsible (TRAC) boom, where the instability occurs because of a sudden change of thickness of the cross section.

TRAC booms (Murphey and Banik, 2011) have been used in solar sails to achieve high packaging efficiency while maintaining desirable structural performance (Banik and Murphey, 2010). Typically, four such booms are arranged along the diagonals of a square sail, coiled around a cylindrical hub during the packaging stage and deployed after the sail is launched into space. An example is the upcoming NASA Near-Earth Asteroid (NEA) Scout mission in which Elgiloy booms are used(Lockett et al., 2020).
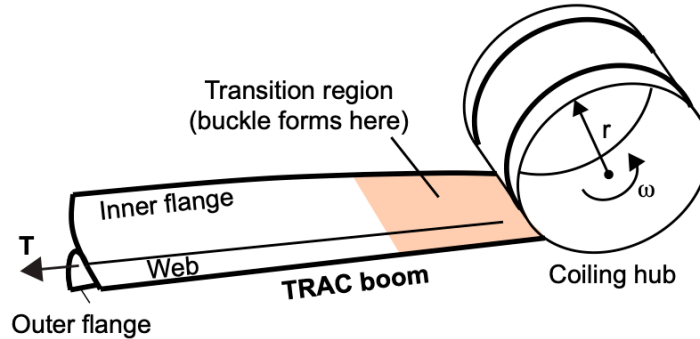
Figure 1: Coiling of TRAC boom.

A TRAC boom, shown in Fig. 1, consists of two cylindrical shells of uniform thickness and transverse curvature (generically known as tape springs, (Miura and Pellegrino, 2020)) bonded along a common edge. The bonded region is called the web, and the two unbonded branches are called the flanges. In the figure, the boom has been flattened at one end and coiled on a cylindrical hub with axis perpendicular to the meridian of the deployed shell. A tip tension is applied to the boom to ensure that the coiled part of the boom and the coiling hub are fully in contact (Wilson et al., 2020).

The region of the boom where contact with the hub is first lost is called the coiling front. The region where the flanges are partially flattened but not yet coiled onto the hub is called the transition region. It is in this region, in the inner flange, that the buckle first appears (Leclerc, 2020; Cox and Medina, 2018) soon after the beginning of the coiling process, see Fig. 2(a). Further coiling of the shell results in the buckle being pushed along the length of the shell. Local material damage has been observed to occur as a result of the buckle formation and propagation.

The above described behavior is also seen in other types of coiling. For ex-
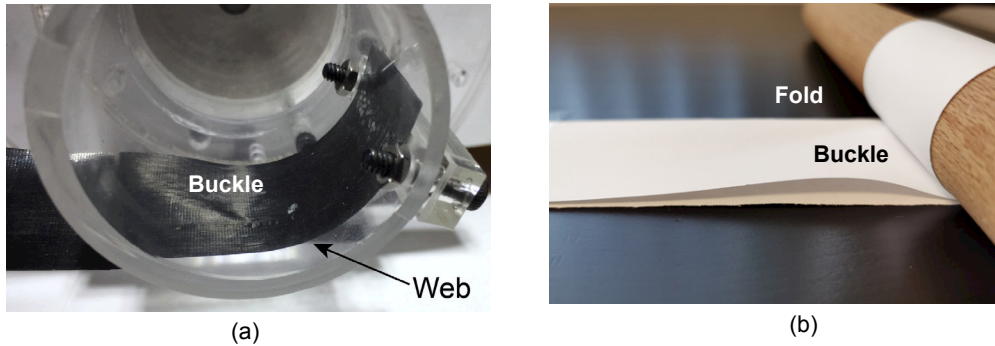
Figure 2: Propagating buckle during coiling of (a) TRAC boom, and (b) folded piece of paper.

ample, when coiling a folded-over sheet of paper using a rolling pin, Fig. 2(b), a buckle forms in the inner half of the sheet. In this case, the buckle amplitude grows when the pin is turned. This buckle is different from Fig. 2(a), as in the paper sheet the two "flanges" are originally flat, but in both cases the buckles can cause material damage, such as delamination and fiber kinking near the web-flange interface of TRAC booms and inelastic creases in the paper sheets.

The present paper is organized as follows. First, a series of high-fidelity numerical simulations of coiling is carried out, to capture the formation of the coiling buckle and provide deeper insights that lead to understanding this type of buckling. It is shown that the shear angle at the edge of the transition region of the shell is an important kinematic parameter to study this problem. Next, the coiling kinematics of the booms are analyzed and a simple analytical model to estimate the critical value of the shear angle is proposed. This model is then used to introduce a simpler buckling problem, in which a buckling analysis of only the transition region of the shell leads

4

to accurate estimates of the critical shear angle. A discussion concludes the paper.

2. Numerical Study of Coiling Instability

This section presents a high-fidelity simulation of coiling that closely follows the buckle formation and evolution.

2.1. Model Description

The ABAQUS finite element model to simulate the coiling of a boom, shown in Fig. 3, was based on Leclerc (2020). The model consists of two main parts: a rigid hub and an elastic, isotropic boom, modeled as two separate tape springs whose nodes are tied in the web region.

Although TRAC booms are mostly built from composite laminates, the present study focuses on isotropic shells in order to avoid the complication of orthotropic shells. Advantages of this simplification are a greater generality of the results and the deeper insight that can be achieved. The formation of buckles in orthotropic booms has been studied in Luo and Pellegrino (2022).

The boom was modeled with 4-node reduced integration Reissner-Mindlin thin shell elements, S4R, with size of 0.67 mm.

The boom was 470 mm long and had the cross section defined in Fig. 3. Its cross-sectional properties were derived from Leclerc (2020): web width $w = 8$ mm, flange thickness $t = 72$ μm, web thickness $2t + t_b = 144$ μm, flange radius $R = 10.6$ mm, and subtended angle $\theta = 105°$. The coiling hub radius was $r = 25$ mm. The Young's modulus of the boom was $E = 70$ GPa and the Poisson's ratio $\nu = 0.2$.
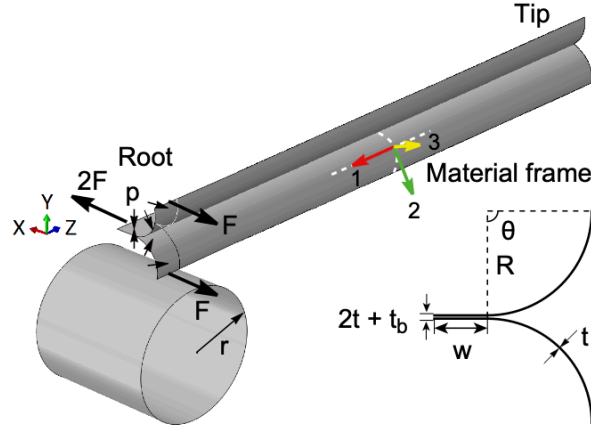
Figure 3: Finite element model for ~~TRAC boom~~ coiling simulation. There are two coordinate systems, X, Y, Z is global and spatially fixed whereas $1, 2, 3$ is curvilinear.

A local material frame aligned with the longitudinal and transverse directions of the boom was defined for the shell elements. The local axes 1,2,3 represent the longitudinal, transverse, and normal directions of the shell, respectively. Therefore, the stresses, strains, and curvatures computed in the local frame are corotational quantities that are invariant under finite rotations during coiling.

The simulation consisted of two main steps: flattening and coiling. First, the root of the boom was flattened by applying two transverse tensions of $F = 25$ N/mm along the edges of the flanges, together with a tension $2F$ on the edge of the web. A flattening pressure of $p = 200$ kPa was applied over an 8 mm long root bonding region. This length is sufficient to maintain alignment of the top and bottom flanges when they are flattened. Once the two surfaces had come into contact, a no-separation contact condition prevented them from separating. At the end of the flattening step, the hub was moved up until it came into contact with the flattened shell. Next, a

tension of 15 N was applied at the tip of the boom to straighten it. Finally, relying on the full bonding of the longeron to the hub, the root of the boom was driven by rotating the hub at a prescribed angular velocity of 0.3 rev/s, forcing the boom to coil around the hub.

The coiling angle is defined as the angle subtended between the root of the flattened boom and the coiling front, where the boom loses contact with the hub.

2.2. Curvature Tensor

To obtain the total curvatures in the coiled configuration, the initial curvature of the undeformed shell was added to the curvature changes provided by Abaqus:

$$\boldsymbol{\kappa} = \begin{pmatrix} \kappa_1 & \kappa_{12} \\ \kappa_{12} & \kappa_2 \end{pmatrix} = \begin{pmatrix} 0 & 0 \\ 0 & -1/R \end{pmatrix} + \begin{pmatrix} \Delta\kappa_1 & \Delta\kappa_{12} \\ \Delta\kappa_{12} & \Delta\kappa_2 \end{pmatrix} \tag{1}$$

where κ_1 and κ_2 are the curvatures in the longitudinal and transverse directions, respectively, κ_{12} is the twist.

With the curvature tensor expressed in the local material frame, its invariants and principal values were obtained. The mean curvature is given by:

$$\bar{\kappa} = \frac{\kappa_1 + \kappa_2}{2}, \tag{2}$$

The Gauss curvature is:

$$\kappa_{\text{Gauss}} = \kappa_1\kappa_2 - \kappa_{12}^2, \tag{3}$$

The minimum principal curvature is:

$$\kappa_{\min} = \frac{1}{2}\left(2\bar{\kappa} - \sqrt{4\kappa_{12}^2 + (\kappa_1 - \kappa_2)^2}\right), \tag{4}$$

7

and the maximum principal curvature is:

$$\kappa_{\max} = \frac{1}{2}\left(2\bar{\kappa} + \sqrt{4\kappa_{12}^2 + (\kappa_1 - \kappa_2)^2}\right).$$ (5)

Note that the principal directions of curvature for the deformed shell do not coincide with the longitudinal and transverse directions of the original, cylindrical surface. They form angles of $\approx 45°$ with the axis of the cylindrical surface.

2.3. Buckle Formation

Contours of the mean curvature in the inner flange of the boom were plotted over the deformed configuration of the structure in Fig. 4, at different stages of coiling.

When the shell had been coiled by about a third of a full revolution, a buckle began to appear near the free edge of the shell, close to coiling front, Fig. 4(a). Immediately after its first appearance, the buckle grew in size and dynamically snapped in the transverse direction, reaching the web-flange interface, Fig. 4(b-c). Then, the buckle slowly grew until reaching a steady state after a full revolution of the hub. This transition corresponds to an increase of the mean curvature from 30 m^{-1} to 42 m^{-1}, in Fig. 4(c-e).

Figure 4(f) shows the final configuration of both the inner and outer flanges (only the outline of the outer flange is shown). Note that the buckle has an elliptical shape. Its long axis forms an angle of roughly 45° against the longitudinal direction. Also note that during the whole coiling process the outer flange did not buckle.

Figures 5(a-b) show the minimum (convex) and maximum (concave) principal curvatures near the buckle, after reaching the steady state. The direc-
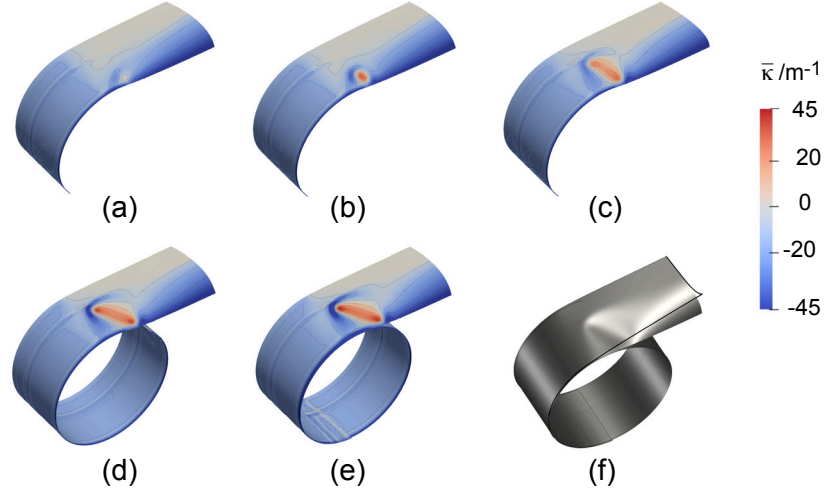
8

Figure 4: Evolution of mean curvature of inner flange in transition region: (a) initiation of buckle at 1/3 hub revolution; (b)-(c) snapping and growth of buckle at 1/3 hub revolution; (d) stable growth of buckle at 1 hub revolution; (e) steady state at 1.5 hub revolution; (f) coiled boom at steady state, showing outline of outer flange and surface of inner flange.

tions of principal curvature are at about 45° to the longitudinal axis of the shell. The contours of the maximum principal curvature indicate that the concave bending is concentrated along the ridge of the buckle. Note that the magnitude of the minimum principal curvature at the upper left corner of the transition region (180 m^{-1}) is almost twice the maximum principal curvature at the same point (100 m^{-1}). The product of the principal curvatures gives the Gauss curvature, plotted in Fig. 5(c). This figure shows that the Gauss curvature is approximately zero, i.e. the surface is almost developable, everywhere except at the two corners of the buckle, where negative values indicate saddle-like local geometries.

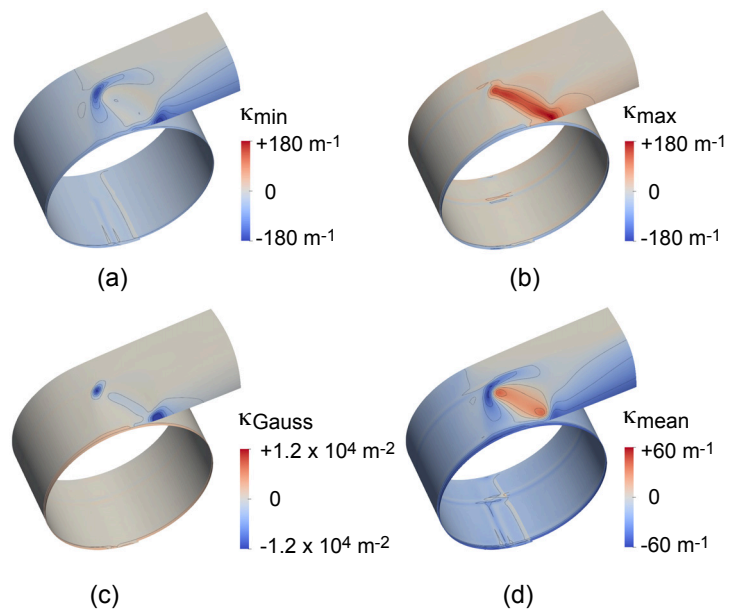The variation during coiling of the minimum principal curvatures at the

Figure 5: Principal values and invariants of curvature tensor at steady state (1.5 hub revolution).

ends of the buckle (points A and B) has been plotted in Fig. 6 and this figure is discussed next. Soon after the start of coiling, the minimum principal curvature is -150 m^{-1} at point A and -24 m^{-1} at point B. When the coiled length of the shell reaches 50 mm, the curvature at B suddenly increases to -91 m^{-1} and then gradually reaches the magnitude of the curvature at A. Both curvatures increase to -194 m^{-1} when the coiled length reaches 160 mm, which corresponds to approximately one full turn.
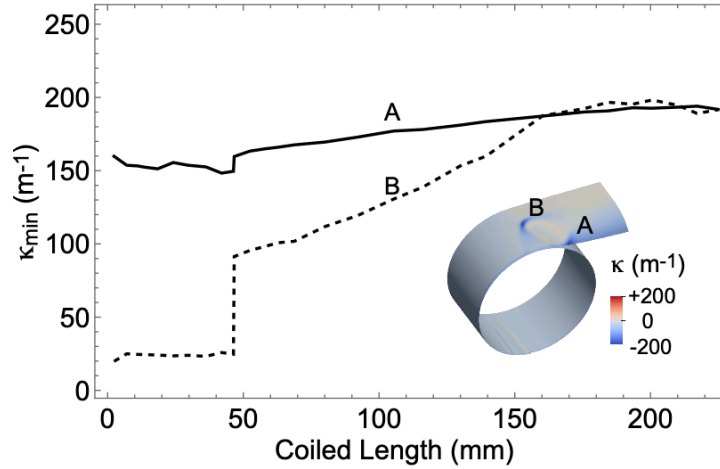

Figure 6: Variation of minimum principal curvature at ends of buckle, showing sudden jump and steady state.

It should be noted that if buckling is avoided, the largest change of curvature would be 94 m^{-1} in the transverse direction, due to flattening the shell, whereas the change of longitudinal curvature would be only 40 m^{-1}. Hence, the present analysis has indicated that the bending stresses in the shell can be double the values estimated from a simple analysis that neglects buckling.

3. Stress Distribution and Shear Deformation

To gain a complementary perspective the in-plane behavior of the inner flange is analyzed. It reveals the compressive stresses that lead to buckling. The longitudinal strain and stress on the mid-surface of the inner flange, as well as the extension of this surface into the web, need to be considered. Note that the flange mid-surface does not coincide with the mid-surface of the web and hence the extension of the flange mid-surface into the web is considered for this part of the study.

It is insightful to study the variation of the longitudinal and shear strains on this surface as the coiling advances. The longitudinal strain at three stages of coiling is shown in Fig. 7. Figure 7(a) shows contours of the longitudinal strain plotted on the undeformed shell geometry, immediately before the formation of the buckle. A simple estimate gives a uniform, compressive strain $\varepsilon_{11} \sim -t/2r$ in the web, whereas the strain in the flange is zero. A comparison of these values to Fig. 7(a) shows that this estimate is not entirely correct, because a small portion of the compression in the web has "leaked" into the flange region, resulting in a relatively small, uniform compression in the middle of the coiled inner flange. Note that the strain at the end of the coiled region becomes non-uniform and forms a boundary layer near the coiling front.

Figure 7(b) shows a snapshot of the same strain component immediately after the formation of the buckle. Comparison with Fig. 7(a) reveals that the zone of highest compression in the transition region, marked by a square, dynamically splits into two separate zones of high (but lower) strain. The two compression zones, marked by squares in Fig. 7(b), are located at the
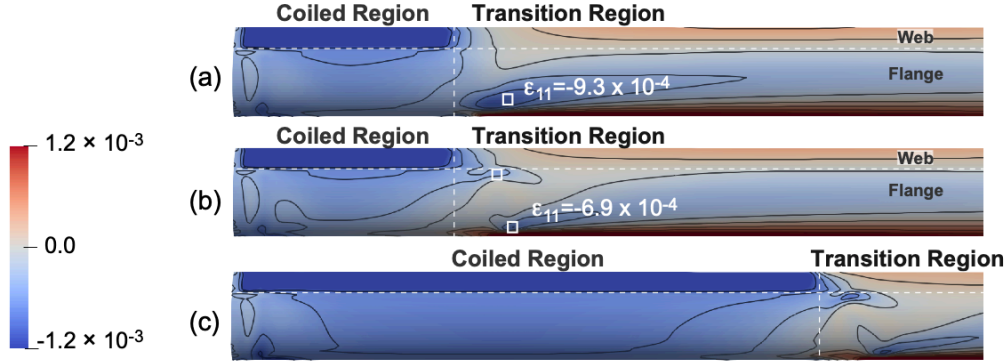
12

Figure 7: Evolution of longitudinal strain ε_{11} on mid-surface of inner flange, plotted on undeformed configuration: (a) immediately before buckling; (b) immediately after buckling; (c) steady state. Interface between web and flange marked by horizontal dashed lines. Interface between coiled and uncoiled (transition) region marked by vertical dashed lines.

web-flange interface and at the free edge of the inner flange. The splitting of the critical compression zone is a result of the buckling of the transition region.

Further coiling of the longeron after the buckling event leads to a slightly higher compression in the transition region, as shown in Fig. 7(c). The buckle propagates quasi-statically, driven by the hub rotation, and gradually reaches a steady-state amplitude. Even though the compression in the coiled web section is relatively high, only a small amount of compression is transmitted into the transition region.

The longitudinal and shear strains at the steady state are compared in Fig. 8. The strain profile in the coiled region is almost uniform, except for boundary layers at both ends of the coiled flange. There is uniform compression with no shear in the middle of the coiled flange, but also rapid

changes of both compression and shear in the boundary layers.

Qualitatively, this result resembles the shear-lag effects that are seen in situations where tension or compression is transmitted through interface shear (Timoshenko and Goodier, 1951; Clyne and Hull, 2019). Hence, the term shear-lag zone will be used to refer to this boundary layer effect.

As noted previously, an important feature of the problem at hand is that the compression in the web leaks to the inner flange through shear-lag. The variation of the compression in the flange results in the shearing of the flange, which can be related to the shear angle at the edge of the transition region of the shell. The in-plane shearing of the shell is the mechanism that leads to the formation of the buckle.

As the steady state is approached, the high compression region in the middle of the inner flange extends in length, whereas the two high shear zones at the ends remain unchanged. This result indicates that the stresses in the coiled region are approximately self-equilibrated and only a small portion of the compression flows into the transition region.

The original shear-lag theory was used to model the stress distribution in open-section, thin-walled beams (Fan, 1939; Timoshenko and Goodier, 1951) and was later extended to the longitudinal stress distribution in short fibers in composite (Clyne and Hull, 2019; Nairn, 1997; Fukuda and Chou, 1981; Wisnom et al., 2007; Liu et al., 2018) and advanced materials (Young et al., 2018; Yu et al., 2018).

The shear-lag theory for a stiff fiber of finite length, L, embedded in an elastic matrix (Clyne and Hull, 2019) provides a second order ordinary differential equation for the variation of the stress, σ_f, along the fiber coordinate
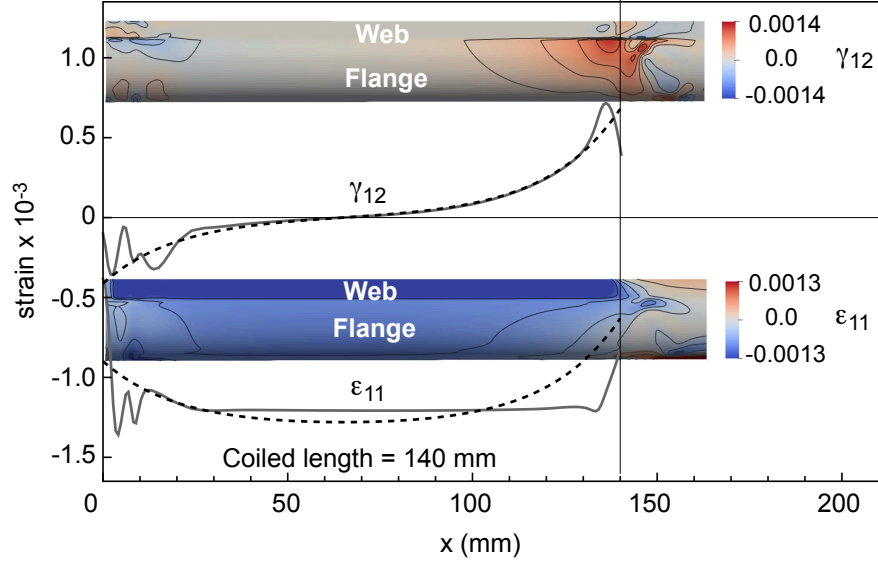
Figure 8: Longitudinal and shear strains along the web-flange interface at steady state. Solid curves are strains from simulation, dashed curves are optimum fits of shear-lag model (Eqs. 7 and 8).

x, with origin at one end of the fiber:

$$\frac{d^2\sigma_f}{dx^2} - \frac{n^2}{\rho_f^2}\sigma_f = -\frac{n^2}{\rho_f^2}E_f\bar{\varepsilon} \tag{6}$$

Here, $\bar{\varepsilon}$ is the overall strain in the fiber direction in the composite, ρ_f, E_f are respectively the fiber radius and the Young's modulus, and n is a dimensionless constant that depends on the fiber and matrix properties. In the present model of boom coiling, the flange corresponds to the fiber and the web corresponds to the matrix.

The solution of Eq. 6, with the end conditions $\sigma_f(0) = \sigma_f(L)$, shows that the fiber stress varies according to the hyperbolic cosine:

$$\sigma_f = E_f\bar{\varepsilon} + A\cosh\frac{n(x - L/2)}{\rho_f} \tag{7}$$

15

whereas the matrix-fiber interface shear stress varies according to the hyperbolic sine:

$$\tau = -\frac{nA}{2}\sinh\frac{n(x-L/2)}{\rho_f} \tag{8}$$

where A is an arbitrary constant that depends on a boundary condition.

Equations 7-8 are converted to strains through $\bar{\varepsilon} = \sigma_f/E_f$ and $\gamma = \tau/G = 2(1+\nu)\tau/E_f$, to obtain:

$$\varepsilon_f = \bar{\varepsilon} + \bar{A}\cosh\frac{n(x-L/2)}{\bar{\rho}} \tag{9}$$

and

$$\gamma = -(1+\nu)n\bar{A}\sinh\frac{n(x-L/2)}{\bar{\rho}} \tag{10}$$

where $\bar{A} = A/E_f$ and $\bar{\rho} = \rho_f/n$.

These expressions are compared in Fig. 8 with the strain components along the coiled web-flange interface, $\varepsilon_{11}, \gamma_{12}$, obtained from the numerical simulation, using the parameters $\bar{\varepsilon} = -1.232 \times 10^{-3}$, $\bar{A} = 1.4 \times 10^{-5}$, $L = 140$ mm, $\bar{\rho} = 17.5$ mm, $\nu = 0.2$, and $n = 1.25$. Note that the sign of the expression for γ has been reversed, to account for the orientation of the local material frame.

The interface shear and longitudinal strain agree with the shear-lag theory in the central part of the coiled region. Larger discrepancies occur near the ends of the coiled region, where the bonding region, on the left, and the buckle, on the right, affect the stress distribution. The maximum relative error for ε_{11} at the two ends is about 25%.

It should be noted that the parameters of the above fitting are for a specific value of L. In other words, the shear-lag model is not an accurate

16

predictive tool. However, it is a useful step towards the development of the predictive model presented in the next section.

The main conclusion from the above study is that the compression in the coiled flange is smaller than in the web, due to leakage through shear-lag. The mismatch in compression between the coiled web and the flange results in a length mismatch and hence in the build-up of shear deformation, starting from the root of the coiled region and increasing along it.

The total shear displacement at the coiling front is denoted by Δ and the relative displacement between the edges of the two flanges is 2Δ, because a similar effect occurs also in the outer flange of the boom (which is in tension and therefore does not buckle). The enlarged view in Fig. 9 shows the relative slip of 2Δ between the inner and outer flanges at the front of the coiled region.
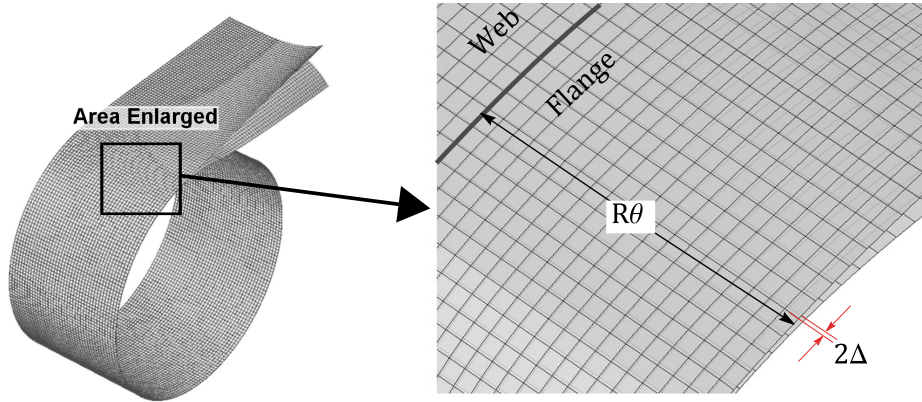

Figure 9: Relative slip between inner and outer flange.

The average shear angle at the coiling front of each flange, γ, can be defined as

$$\gamma = \frac{\Delta}{R\theta} \tag{11}$$

17

where $R\theta$ is the width of the flanges.

Detailed estimates of γ can be obtained from the coiling simulation and can be compared to the extreme value of Eq. 10. Since the interface shear is related to the magnitude of compression prior to buckling, the value of γ at the coiling front is a key variable for the present study, which is further discussed in the following.

4. Analytical Model of Coiling

This section presents a simple, nonlinear spring model of the buckle formation. The underlying mechanism is the length mismatch between the flanges and the web, identified in Section 3, for which two limiting cases are identified. Then, the maximum shear strain γ in the shear-lag zone of the coiled shell is expressed in terms of the free length of two linear extensional springs representing the coiled web and flange, as well as rotational stiffnesses that represent the shear lag zone.

4.1. Coiling Kinematics

The study in the previous section has shown that the buckling during coiling of a TRAC boom is caused by the shear angle at the front of the coiled region, resulting from the incompatible coiling kinematics of the web and flanges.

It is convenient to consider the extreme cases of booms in which the flanges are perfectly glued together, Fig. 10(a), or the web has been sliced through the middle, Fig. 10(b). In the first case, the inner and outer flanges are respectively under compression and tension. The neutral surface, which corresponds to the mid-surface of the web, is stress free and hence there is zero relative slip between the inner and outer parts of the boom. In the

18

second case, the two halves of the web are free to slip against each other, like the flanges, and hence there are two separate neutral surfaces for the inner and outer parts of the boom. Therefore, the two parts of the boom coil as separate shells, whose coiling radii differ by a flange thickness, t, thus inducing a relative slip between the inner and outer flange.

In both of the cases outlined above, there would be no compression on the mid-surface of the shells, and therefore no buckling would occur.

Next, consider the coiling of a TRAC boom. This case is intermediate between the two limiting cases discussed above and is shown in Fig. 10(c). To accommodate the mismatch between the two neutral surfaces, high shear stress develops at the web-flange interface, allowing a portion of the compression at the inner half of the web to be leaked into the inner flange through the shear-lag mechanism. Compared to the separate coiling scenario, the slip between the two flanges is smaller in the actual coiling process. More importantly, it is directly related to the shear stiffness of the shell. Differently from the separate coiling, the slip must be zero at the web-flange interface for continuity of the displacement field. Thus, the previously defined shear angle, γ, appears naturally as the work conjugate of the shear stress in the shear-lag region, and is shown in Fig. 10(c).

4.2. Shear Angle

4.2.1. Upper Bound on Maximum Slip

The maximum possible slip between the inner and outer flanges is determined by the separate coiling scenario of Fig. 10(b). In this case, the mid-surface of each flange is a neutral surface and hence does not change its longitudinal
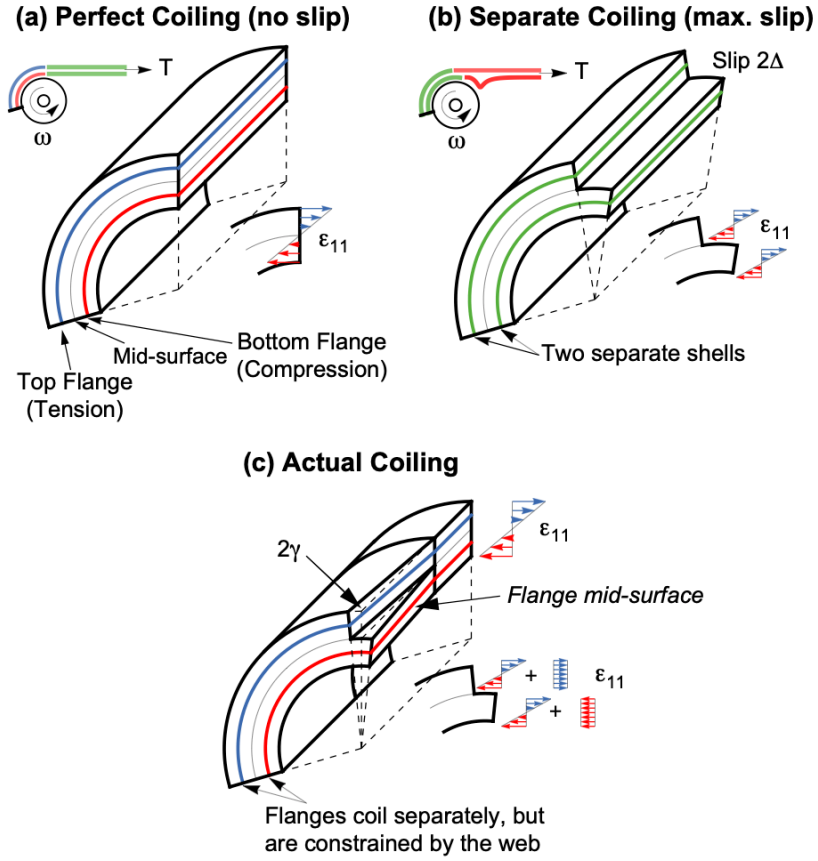
Figure 10: Schematic showing: (a) perfect coiling of shell made by gluing together two identical shells; (b) coiling of two separate shells glued together at one end; (c) actual coiling.

length. The lengths of the coiled inner and outer flanges are respectively:

$$\left(r + \frac{t}{2}\right)\phi, \text{ and } \left(r + \frac{3t}{2}\right)\phi \tag{12}$$

where ϕ is the coiling angle.

Hence, the relative slip between the two flanges is $2\Delta_{\max} = \phi t$ and hence

the maximum possible shear angle is given by:

$$\gamma_{\max} = \frac{\Delta_{\max}}{R\theta} = \frac{\phi t}{2R\theta} \tag{13}$$

This equation shows that the upper bound on the relative slip, as well as the shear angle between the inner and outer flanges, increase proportionally to the hub rotation. They are also proportional to the flange thickness, t, as well as the inverse of the flange width, $1/R\theta$.

Of course, in reality the actual shear angle cannot grow indefinitely, as predicted by Eq. 13. As it was observed in the numerical simulations, the strains and curvatures reach a steady state after buckling occurs.

4.2.2. Spring Model

A set of linear springs, inspired by the shear-lag model, can capture the leakage of compression from the web to the flange, Fig. 11. This model consists of two extensional springs, ab and $a'b'$, which capture the average shortening of the coiled inner half of the web and of the inner flange, respectively. These springs have strains $\varepsilon_w, \varepsilon_f$ and stiffnesses k_w, k_f, respectively. To capture the shear-lag mechanism and allow some compression to leak from the web to the inner flange, the springs are connected by the rigid rods aa' and bb' with rotational springs at a and b. Hence, the compression in spring ab is transmitted to the spring $a'b'$ through the rotation of aa' and bb', representing the shearing of $a'ab$ and abb'. The shear stiffness is captured by the rotational springs k_a, k_b, with rotations γ_a, γ_b. L_s is the length of $a - a'$ and $b - b'$, and L is the *coiled length* of the boom.

The above-described model can be used to determine γ_b as a function of the coiled length L.
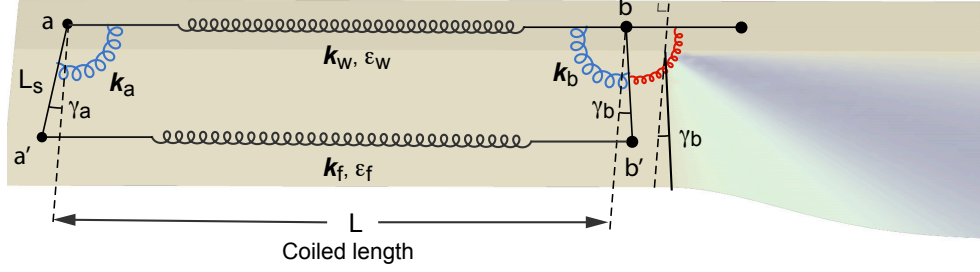
21

Figure 11: Spring model overlaid on schematic of uncoiled inner flange mid-surface.

Coiling induces a compressive strain in the web, which at the location of the flange mid-surface, shown in Fig. 10(c), has the value:

$$\varepsilon_0 = -\frac{t}{2r} \tag{14}$$

Due to the compression leakage to the flange, represented by spring $a' - b'$, the strain in the spring representing the web is reduced to

$$\varepsilon_w = \varepsilon_0 + \Delta\varepsilon \tag{15}$$

where $\Delta\varepsilon$ denotes the leakage of the longitudinal strain due to the rotational spring k_b. Associated with $\Delta\varepsilon$ is a force in the spring $a - b$, denoted by ΔF, and an equal and opposite force in the spring $a' - b'$.

Finding γ_b requires the solution of a statically indeterminate problem, which involves the combination of kinematic compatibility, static equilibrium, and constitutive relations to find a unique solution.

The compatibility condition between the extensions due to the rotations of aa' and bb' and the difference in the contraction of springs $a - a'$ and $b - b'$ is:

$$L_s\gamma_a + L_s\gamma_b = L(\varepsilon_f - \varepsilon_w) \tag{16}$$

22

The constitutive relations for the two extensional springs are:

$$\Delta F = k_w L \Delta \varepsilon, \text{ and } -\Delta F = k_f L \varepsilon_f \qquad (17)$$

Equating these relations eliminates ΔF and gives:

$$\varepsilon_f = -\frac{k_w}{k_f} \Delta \varepsilon \qquad (18)$$

On the other hand, ΔF applies a moment on the rotational springs, and hence is related to the shear angles by:

$$k_a \gamma_a = \Delta F L_s, \quad k_b \gamma_b = \Delta F L_s \qquad (19)$$

Substituting Eq. 15 and Eq. 18 into Eq. 16, then combining with Eq. 19, and solving for γ_b and $\Delta \varepsilon$ gives:

$$\gamma_b = -\frac{L L_s}{\left(1 + \frac{k_b}{k_a}\right) L_s^2 + \left(\frac{1}{k_w} + \frac{1}{k_f}\right) k_b} \varepsilon_0 \qquad (20)$$

$$\Delta \varepsilon = -\frac{\varepsilon_0}{\left(\frac{1}{k_a} + \frac{1}{k_b}\right) k_w L_s^2 + \frac{k_w}{k_f} + 1} \qquad (21)$$

where it should be recalled that ε_0 is given by Eq. 14.

To check the validity of Eqs. 20-21, the limiting cases where k_a and k_b tend to 0 and ∞ are considered. When $k_a = k_b = k \to 0$, $\gamma_b \to L\varepsilon_0/2L_s$ and $\Delta \varepsilon \to 0$, which corresponds to the case of rotational springs that cannot transmit any moment (i.e., separate coiling) gives: $\Delta_{\max} = L\varepsilon_0$. When $k_a = k_b = k \to \infty$, i.e. the rotational springs are rigid, $\gamma_b \to 0$, and $\Delta \varepsilon \to -\varepsilon_0/(1 + k_w/k_f)$, which corresponds to the inner flange transmitting the maximum possible amount of compression. In practice, the compression in the coiled inner flange is always smaller than the compression in the coiled web, as observed in the simulations.

Finally, it is noted that the spring constants are related to the Young's modulus of the boom by the relations:

$$k_w = E\frac{wt}{L}, \text{ and } k_f = E\frac{\theta Rt}{L} \tag{22}$$

The rotational stiffnesses k_a, k_b are related to the shear modulus of the boom, G, and the non-uniformity of the shear stress along the web-flange interface, Fig. 8, can be captured by introducing two correction coefficients, η_a and η_b:

$$G\gamma_{a,b} = \frac{\bar{\tau}}{\eta_{a,b}} = \frac{\Delta F}{\eta_{a,b}L_0 t}, \text{ with } \eta_{a,b} \leq 1 \tag{23}$$

Here L_0 denotes the length of the shear-lag zone, defined as the length of the interface with a shear strain greater than 10% of the maximum shear strain near the coiling front, see Fig. 8. $\bar{\tau}$ is the average shear stress in the shear-lag zone.

Combining Eq. 23 with Eq. 19 to eliminate ΔF, gives the spring constants for the shell prior to buckling:

$$k_a = \eta_a t L_s L_0 G, \text{ and } k_b = \eta_b t L_s L_0 G \tag{24}$$

Substituting the expressions for k_w and k_f, Eq. 22 and Eq. 18, into the expression for γ_b in Eq. 20 gives:

$$\gamma_b = -\frac{2}{(1 + \eta_b/\eta_a)L_s/L + L_0(1/w + 1/\theta R)\eta_b G/E}\varepsilon_0 \tag{25}$$

and substituting $E/G = 2(1 + \nu)$ gives:

$$\gamma_b = -\frac{2(1+\nu)}{2(1+\nu)(1 + \eta_b/\eta_a)L_s/L + L_0(1/w + 1/\theta R)\eta_b}\varepsilon_0 \tag{26}$$

where ν is the Poisson's ratio of the material.

24

Every quantity in this expression for γ_b is evaluated using the properties of the boom, except for L_s which is taken as a calibration parameter, between 0 and $w + \theta R$, and η_a, η_b which are also calibration parameters.

4.2.3. Shear Angle during Coiling

The expression for γ_b in Eq. 25 can be rewritten as:

$$\gamma_b(L) = \frac{1}{\Omega/L + \Psi} \left(\frac{t}{2r} \right) \tag{27}$$

with

$$\Omega = (1 + \eta_b/\eta_a)L_s \tag{28}$$

and

$$\Psi = L_0 \left(1/w + 1/\theta R \right) \eta_b G/E \tag{29}$$

Note that both of these parameters are only dependent on the material properties and the shell geometry.

To study the variation of γ_b during coiling, the length of the coiled region of the boom, $L = \phi r$, can be taken as the independent variable. For small values of L, γ_b increases linearly and remains close to its upper bound (Eq. 13, since $\Omega \approx R\theta$):

$$\gamma_b \approx \frac{1}{\Omega} \left(\frac{t}{2r} \right) L \tag{30}$$

When L is large, γ_b reaches a plateau (steady state), given by:

$$\gamma_b \approx \frac{1}{\Psi} \left(\frac{t}{2r} \right) \tag{31}$$

This result agrees with the previous observation that the coiling of booms always reaches a steady state.

To account for the effect of buckling, two different values of k_b are used in the expression for γ_b. This corresponds to decreasing η_{buckled} to the value of η_b in Eqs 28-29. A specific value of η_{buckled} is obtained by calibration with the high-fidelity coiling simulations; in the present case η_b decreased from 0.53 to 0.47. As a result, the variation of γ_b with L will show a jump.

The variation of γ_b predicted by this model is compared in Fig. 12 with the ~~he~~ maximum shear strain obtained from the high-fidelity simulation of boom coiling. In this figure, the circles denote values obtained from the simulation, whereas the solid curves are the optimum fits using the spring model of Eq. 27. The model parameters are given in Table 1.
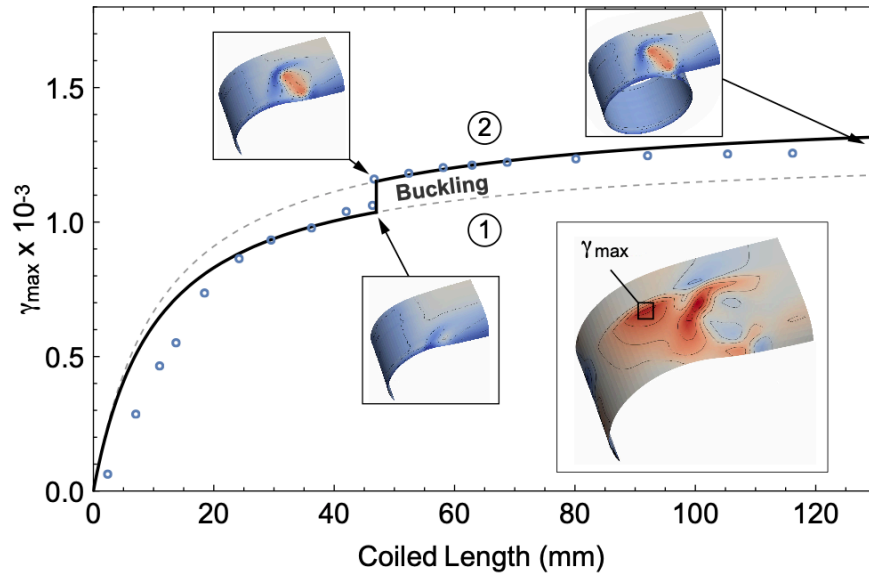

Figure 12: Evolution of maximum shear strain, γ_{max}, against coiled length. Circles are from coiling simulation. Curves are optimum fits of spring model.

This comparison has shown that the spring model is capable of matching the maximum shear angle γ obtained in the simulations. Importantly, it

Fixed Parameters	Value	Model Parameters	Value
Young's modulus, E	70 GPa	L_s	7.85 mm
Poisson's ratio, ν	0.2	L_0	$\sqrt{3}R\theta$
Web width, w	8 mm	η_a	1
Flange radius, R	10 mm	η_b	0.53
Subtended angle, θ	105°	η_{buckled}	0.47
Flange thickness, t	72 μm	γ_c	0.00106
Hub radius, r	25 mm		

Table 1: Parameters of spring model.

has been shown that γ reaches a plateau, regardless of whether the flange buckling occurs or not (see curves 1 and 2 in Fig. 12). It has also been shown that when the buckle forms there is a jump in the value of γ, due to the stiffness drop of the rotational spring. In the present case, a jump of about 21.5% occurred at the buckling limit $\gamma = \gamma_c$ and the value of γ_{max} instantaneously increased by about 20%.

The spring model has been expressed in terms of six model parameters, listed in the second column of Table 1. In general, these parameters can be estimated as follows. The first parameter is the length of the rigid rods between the two springs and can be estimated as $L_s = 0.5R\theta$. The second parameter is the length of the shear-lag zone, which can be estimated as $L_0 = \sqrt{3}R\theta$ for a wide range of flange thicknesses and cross section geometries. The next three parameters have the values $\eta_a \sim 1$ and $\eta_b \sim \eta_{\text{buckled}} \sim 0.5$. The final model parameter, γ_c, is the critical buckling shear angle, and can be obtained from the simple shell buckling simulation presented in Section 5.

5. Buckling of Transition Region

Since the overall mechanism for buckling during coiling has been both explained and modeled, the study now focuses on the buckling event itself. The present objectives are to understand the type of buckling and to estimate the critical shear angle, at which the buckle forms.

Since the boom has been deformed into an irregular geometry (i.e. neither axisymmetric nor cylindrical), its buckling and post-buckling responses can only be studied through numerical models. However, the high-fidelity coiling simulations of Section 2 can be avoided by switching from the Lagrangian approach, previously adopted, to an Eulerian approach. In other words, regardless of the location of the material points during coiling, a fixed view of the shell can be adopted, in order to focus on the stability of a specific region of interest.

The <u>ploy region</u> of a coiled boom is defined as the region in which the boom transitions from one cylindrical surface (deployed configuration) to another cylindrical surface (coiled configuration). The length of the ploy region for an isotropic tape spring can be calculated from (Seffen et al., 2019):

$$L_p = \frac{1}{\sqrt{70}} \frac{b^2}{\sqrt{Rt}} \tag{32}$$

where b is the arc length of the cross-section.

For a shell formed by the inner flange and the web of the boom, depending on the choice made for b, Eq. 32 gives $L_p = $ 52-206 mm. These values were obtained respectively for b equal to the arc length of the flange of the boom and twice this value, to reflect the fact that the edge boundary conditions for the shell are different from Seffen et al. (2019). Since it has been noted by

Rakow and Reedy (2022) that the cross-sectional variation approaches the deployed cross-section asymptotically over the length L_p, it is unnecessary to consider the full ploy length and hence in the present study $L_p = 90$ mm was assumed.

The analysis was divided into two parts. The first part computed the flattening of the edge of the region of interest, using the Abaqus Explicit solver. Only the inner flange was included in the region of interest, and the simulation started in the deployed configuration. The second part of the analysis computed the buckling of the region of interest, modeling the influence of the coiled and fully-deployed parts of the boom through the use of suitable boundary conditions and loads.

As in Section 2, S4R shell elements were used for the analysis. A uniform square mesh with element size of 0.5 mm was chosen for the transition region and a non-uniform coarse mesh was used elsewhere, to reduce the scale of the computation. Instead of including the web in the analysis, a clamped boundary condition was imposed along the edge of the flange.

The left edge of the inner flange was flattened by prescribing the transverse and vertical displacements, u_x and u_y, of the corner node, see Fig. 13b. Note that at the end of the flattening stage, the reaction force F is negative. This means that the corner is under longitudinal tension before the buckle begins to form. This result matches the coiling simulation, where the free edge of the inner flange is always under tension. In the following step, a shearing deformation of the edge was imposed by increasing the longitudinal displacement, Δ, of the corner node, Fig. 13c. The buckling and post-buckling responses of the transition region were characterized by

29

the relation between the change in reaction force relative to the end of the flattening step, ΔF, and the corner displacement, Δ.
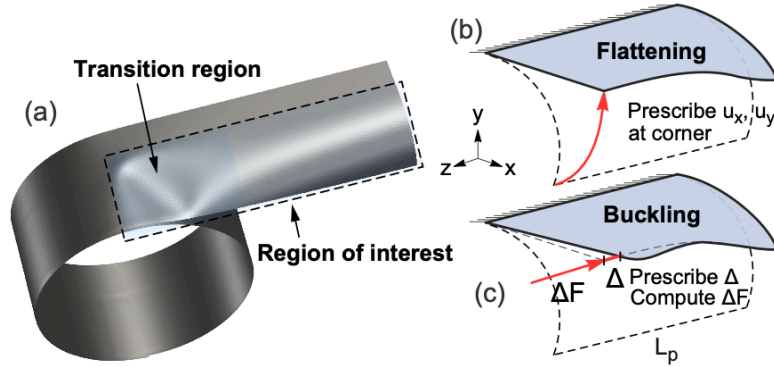

Figure 13: Schematic of buckling simulation: a) region of interest; b) configuration for flattening; c) configuration for buckling.

The relation between ΔF and Δ has been plotted in Fig. 14, which shows that, under load control, the system undergoes snap-through buckling and dynamically snaps to point C after reaching point A. The spontaneous jump from point A to C is consistent with the sudden jump of the shear angle, shown in Fig. 12. In addition, the reduction of the transition region stiffness due to buckling corresponds to the reduction of slope from line OA to line OC (secant stiffness). As the corner is pushed longitudinally, the buckle keeps growing in magnitude, but the process remains stable (e.g., point C to point D in Fig. 14).

The concept of "Maxwell load", based on an energy criterion (Kyriakides, 1993), is an established tool for the analysis of problems involving the propagation of instabilities. For the load-displacement curve shown in Fig. 14, the Maxwell load can be found by drawing a horizontal line such that the
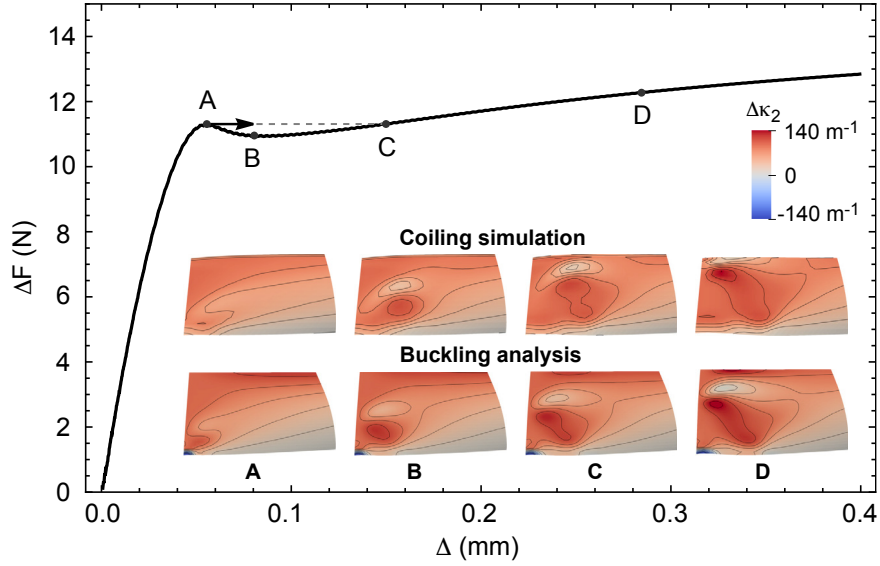
Figure 14: Corner load-shortening curve from buckling simulation. Comparisons between transverse curvature change, $\Delta\kappa_2$, from coiling vs. buckling simulation shown as snapshots.

areas enclosed by the curve, above and below the line, are equal. The end point of intersection between the line and the curve marks the minimum load under which the buckle can propagate quasi-statically. Note that this propagation load is lower than the value of ΔF at point A in the figure, which is the threshold for the buckle to initiate. This instantaneous, unstable propagation of the buckle occurs in the transverse direction, and the buckle propagation in the longitudinal direction is completely passive and is driven by the coiling hub rotation.

The upper row of snapshots in Fig. 14 shows the contours of the transverse curvature changes during the coiling simulation of the complete boom. The lower row shows the corresponding results from the buckling simulation. By comparing the two sets of results, it is clear that the simplified model cap-

tures quite accurately the buckling of the transition region during coiling. Note that the columns A, B, C, and D in the snapshots refer to the corresponding points on the load-shortening curve. They represent the buckle initiation, spontaneous and unstable (snap-through) buckling, end of spontaneous buckling, and stable growth of the buckle respectively. It is therefore concluded that the buckling of the transition region is a snap-through instability (Bazant and Cedolin, 1991).

The critical shear angle corresponds to point A in Fig. 14, where $\Delta_A = 0.055$ mm. However, estimating the critical shear angle for the spring model requires some care because the assumptions of the spring model and the buckling model, presented in this section, are different. The spring model assumes a linear deformation of the coiling front of the shell, whereas no such restriction is imposed in the buckling model. Therefore, the critical shear angle for the spring model is computed as the least-square-error fit to the edge deflection corresponding to point A of the buckling simulation, as shown in Fig. 15.

This estimate leads to a critical shear angle of 0.00114 rad, which differs by only 6% from the maximum shear strain of $\gamma_{max} = 0.00106$ obtained from the coiling simulation, Table 1.

6. Discussion and Conclusions

This study of coiling instabilities in linear-elastic isotropic booms that consist of two curved flanges bonded together to form a flat web of double thickness, has provided much insight into the formation and propagation of coiling buckles in TRAC booms, together with models that predict the
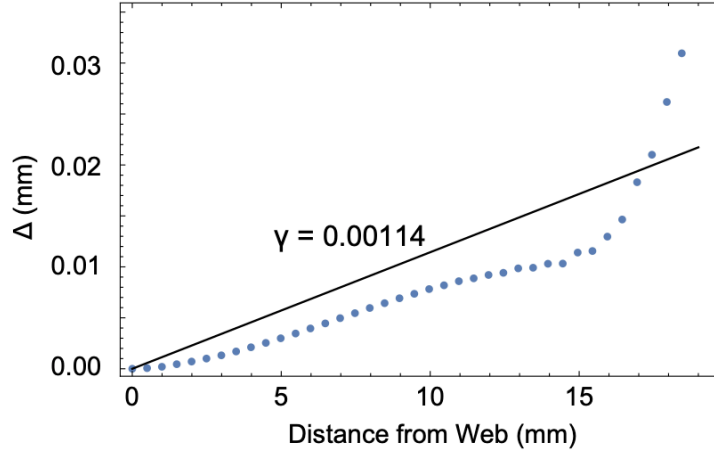
32

Figure 15: Linear fit to nonlinear edge deflection obtained from buckling simulation.

amplitude of the buckles.

It has been shown that the coiling leads to longitudinal compression of the inner flange mid-surface. This compression can lead to the formation of a buckle in the transition region between the fully coiled and fully deployed parts of the inner flange. The buckle formation is a snap-through instability that is associated with a jump discontinuity in almost every observable variable, including the coiling torque and, once formed, the buckle grows in amplitude until it reaches a steady state.

The mid-surface compression of the inner flange is uniform in the central part of the coiled region, and decreases near the coiling front. The corresponding longitudinal strain varies in the same way. The shear strain in the mid-surface of the inner flange vanishes at the center of the coiled region. It increases exponentially towards the coiling front where it reaches its largest magnitude.

The maximum value of the shear strain in the inner flange, at the coiling

front, has been estimated with good accuracy using a discrete spring model, whose properties are related to the Young's modulus and shear modulus of the inner flange, the width of the web and the transverse arc length of the inner flange, and the coiled length of the boom. This model has shown that the shear strain at the coiling front of the inner flange tends to reach a limit when the coiled length of the boom is increased. The asymptotic limit is proportional to the ratio of the flange thickness to the radius of coiling.

The value of the coiling front shear strain at which the buckle first forms can be predicted by carrying out a buckling analysis on a relatively small region of interest of the shell, which captures the deformation of the transition region of the inner flange.

The snap-through buckling and the formation of a localized buckle correspond to a decrease in the stiffness of the spring model and a corresponding increase of the shear strain at the coiling front. The maximum shear strain predicted by the spring model can then be used to determine the amplitude of the buckle, using the buckling analysis.

Although the present study has focused on a specific TRAC boom cross-section, the insight that has been gained is applicable to coilable shell structures in general. Different boom cross-sections, orthotropic composite shells, also with thickness variations introduced through ply drops, could all be studied as extensions of the present study.

Acknowledgments

References

J. Banik, T. Murphey, 2010. Performance validation of the triangular rollable and collapsible mast, 24th Annual AIAA/USU Conference on Small Satellites, SSC10-II-1.

Z. P. Bazant, L. Cedolin, 1991. Stability of structures: elastic, inelastic, fracture and damage theories. Oxford University Press. `doi:https://doi.org/10.1142/7828`

T. W. Clyne, D. Hull, 2019. An Introduction to Composite Materials, Cambridge University Press. `doi:https://doi.org/10.1017/CBO9781139170130`

K. Cox, K. Medina, An investigation of inner flange buckling in furlable composite booms, in: Proceedings of the American Society for Composites—Thirty-third Technical Conference, 2018. `doi:https://doi.org/10.12783/asc33/26162`

H. T. Fan, 1939. A study of "shear lag" phenomenon in a stiffened flat panel by photoelastic methods. Master's thesis, California Institute of Technology. `doi:https://doi.org/10.7907/WANC-TP12`

H. Fukuda, T.-W. Chou, 1981. An advanced shear-lag model applicable to discontinuous fiber composites, Journal of Composite Materials 15 (1), 79–91. `doi:https://doi.org/10.1177/002199838101500107`

J. K. Good, D. R. Roisum, 2008. Winding: machines, mechanics and measurements, DEStech Publications, Lancaster, PA. ISBN: 193207869X.

A. D. Hasanyan, C. Leclerc, S. Pellegrino, 2020. Interface failure analysis of triangular rollable and collapsible (TRAC) booms, in: AIAA Scitech Forum 2020, p. 0694. `doi:https://doi.org/10.2514/6.2020-0694`

S. Kyriakides, 1993. Propagating Instabilities in Structures. In: Advances in Applied Mechanics, Edited by J.W. Hutchinson and T.Y. Wu, 30, pp. 67-189, Academic Press, Boston, MA. `doi:https://doi.org/10.1016/s0065-2156(08)70174-1`

C. Leclerc, 2020. Mechanics of ultra-thin composite coilable structures, Ph.D. thesis, California Institute of Technology. `doi:https://doi.org/10.7907/X60S-BR30`

J. Liu, W. Zhu, Z. Yu, X. Wei, 2018. Dynamic shear-lag model for understanding the role of matrix in energy dissipation in fiber-reinforced composites, Acta Biomaterialia, 74, 270–279. `doi:https://doi.org/10.1016/j.actbio.2018.04.031`

T.R. Lockett, J. Castillo-Rogez, L. Johnson, J. Matus, J. Lightholder, A. Marinan and A. Few, 2020. Near-Earth Asteroid Scout flight mission. IEEE Aerospace and Electronic Systems Magazine, 35(3), pp. 20-29. `doi:https://doi.org/10.1109/MAES.2019.2958729`

W. Luo, S. Pellegrino, 2022. Propagating instabilities in coilable booms. AIAA SciTech Forum 2022, p. 0407. `doi:https://arc.aiaa.org/doi/abs/10.2514/6.2022-0407`

K. Miura, S. Pellegrino, 2020. Forms and Concepts for Lightweight Structures, Cambridge University Press. `doi:https://doi.org/10.1017/9781139048569`

T. W. Murphey, J. Banik, 2011. Triangular rollable and collapsible boom, US Patent 7,895,795 (Mar. 1 2011).

J. A. Nairn, 1997. On the use of shear-lag methods for analysis of stress transfer in unidirectional composites, Mechanics of Materials, 26 (2), 63–80. `doi:https://doi.org/10.1016/S0167-6636(97)00023-9`

T. L. Power, S. Kyriakides, 1994. Localization and propagation of instabilities in long shallow panels under external pressure, ASME Journal of Applied Mechanics 61, 755-763. `doi:https://doi.org/10.1115/1.2901551`

A.S. Rakow, R. Reedy, 2022. Predicting ploy length of high-strain composite slit-tubes and tape-springs. AIAA Scitech Forum 2022, p. 2266. `doi:https://arc.aiaa.org/doi/abs/10.2514/6.2022-2266`

D. R. Roisum, 1984. The Mechanics of Winding. Tappi Press. ISBN 0898522811.

K. A. Seffen, B. Wang, S. D. Guest, 2019. Folded orthotropic tape-springs. Journal of the Mechanics and Physics of Solids, 123, 138-148. `doi:https://doi.org/10.1016/j.jmps.2018.09.017`

S. P. Timoshenko, J. N. Goodier, 1951. Theory of Elasticity, 2nd Edition, McGraw Hill.

L. Wilson, E. Gdoutos, S. Pellegrino, 2020. Tension-stabilized coiling of isotropic tape springs. International Journal of Solids and Structures, 188-189, 103-171.

M. R. Wisnom, K. D. Potter, N. Ersoy, 2007. Shear-lag analysis of the effect of thickness on spring-in of curved composites, Journal of Composite Materials, 41 (11) (2007) 1311–1324. `doi:https://journals.sagepub.com/doi/10.1177/0021998306068072`

R. J. Young, M. Liu, I. A. Kinloch, S. Li, X. Zhao, C. Vallés, D. G. Papageorgiou, 2018. The mechanics of reinforcement of polymers by graphene nanoplatelets, Composites Science and Technology, 154, 110–116. `doi:https://doi.org/10.1016/j.compscitech.2017.11.007`

Z. Yu, J. Liu, X. Wei, 2018. Unraveling crack stability and strain localization in staggered composites by fracture analysis on the shear-lag model, Composites Science and Technology, 156, 262–268. `doi:https://doi.org/10.1016/j.compscitech.2017.12.035`